P. J. Newton

G. D. Lock

Department of Mechanical Engineering,
University of Bath,
Bath, UK

S. K. Krishnababu

H. P. Hodson

W. N. Dawes

Department of Engineering,
University of Cambridge,
Cambridge, UK

J. Hannis

Siemens Industrial Turbomachinery Ltd.,
Lincoln, UK

C. Whitney

Alstom Power Technology Centre,
Leicester, UK

Heat Transfer and Aerodynamics of Turbine Blade Tips in a Linear Cascade

Local measurements of the heat transfer coefficient and pressure coefficient were conducted on the tip and near tip region of a generic turbine blade in a five-blade linear cascade. Two tip clearance gaps were used: 1.6% and 2.8% chord. Data was obtained at a Reynolds number of 2.3×10^5 *based on exit velocity and chord. Three different tip geometries were investigated: A flat (plain) tip, a suction-side squealer, and a cavity squealer. The experiments reveal that the flow through the plain gap is dominated by flow separation at the pressure-side edge and that the highest levels of heat transfer are located where the flow reattaches on the tip surface. High heat transfer is also measured at locations where the tip-leakage vortex has impinged onto the suction surface of the aerofoil. The experiments are supported by flow visualization computed using the CFX CFD code which has provided insight into the fluid dynamics within the gap. The suction-side and cavity squealers are shown to reduce the heat transfer in the gap but high levels of heat transfer are associated with locations of impingement, identified using the flow visualization and aerodynamic data. Film cooling is introduced on the plain tip at locations near the pressure-side edge within the separated region and a net heat flux reduction analysis is used to quantify the performance of the successful cooling design.* [DOI: 10.1115/1.2137745]

1 Introduction

In a gas turbine a gap between the rotating blade tip and the stationary casing is needed to allow relative motion. In an unshrouded turbine stage this tip gap is nominally of the order 1% of blade height. The difference in pressure between the pressure and suction aerofoil surfaces drives hot mainstream flow through the gap between the tip of the rotating blade and the surrounding casing. The leakage is essentially axial, i.e., orthogonal to the casing motion. The flow separates at the pressure-side edge and, depending on the blade thickness, reattaches downstream. At the exit of the clearance the mixed-out flow meets the mainstream on the suction side and rolls up into a vortex. Geometric changes to the blade tip can be effective in reducing the leakage flow. A current design features a recessed tip, known as a squealer, where the tip gap can be made smaller without risk of significant tip contact with the casing. In addition to mechanical benefits, the recess also acts as a labyrinth seal, increasing resistance to the flow.

This tip leakage has a detrimental effect on the stage efficiency. Aerodynamic losses occur due to viscous effects within the tip gap itself and due to mixing losses when the leakage flow interacts with the passage flow. Furthermore there is a reduction in work output from the stage as the leakage flow exits unturned, though some of this work may be recovered in latter stages of a multistage turbine. Booth et al. [1] estimated that a tip clearance gap of 1% blade height potentially leads to losses of 1%–3% in stage efficiency. Manufacturing tolerances, centrifugal expansion and dissimilarity between the thermal loading of the blade row and casing leads to nonuniform clearance gaps around the annulus. Geometric changes to the tip profile (such as squealers or cavities) are commonly used to improve stage performance.

Another important consequence is the deterioration of the blade tip surface due to regions of high local heat transfer in the narrow gap. The thinning of the pressure-side boundary layer as the leakage flow accelerates into the tip gap causes a rapid rise in heat transfer on entry to the tip gap. Additionally the high velocity mixing within the tip gap itself causes some of the highest heat transfer rates on the blade in what is a very difficult region to cool effectively. The high velocity leakage flow exiting the tip gap creates leakage vortices which impinge onto the suction surface and create further localized regions of elevated heat transfer. All of these factors make the blade tip one of the regions in the engine that limits performance and demands frequent inspection. It is, therefore, important to understand the aerodynamics and heat transfer within the gap in order to introduce new tip designs that might reduce the leakage flow.

This paper presents experiments and computations relating to such flows modeled using generic, blade-tip geometries in an engine-simulated environment. No relative motion between the tip and casing is present in this study and it is assumed that the flow through such clearances is essentially driven by pressure difference. This has been verified by Mayle and Metzger [2] and later Srinivasan and Goldstein [3] who have shown that the shear-stress distribution within such gaps is unaffected by relative motion at 100% engineering equivalent speed and that no measurable change in heat transfer occurred for tip-gap to chord ratios greater than 0.86%.

A review of research quantifying the losses and heat transfer associated with tip clearance flow is provided by Bunker [4]. Much of the early work used idealized models, e.g., Kim and Metzger [5] and Chen et al. [6]. More recently much data has been published using linear cascades: Bunker et al. [7] measured heat transfer for sharp and radiused-edged blades for different clearance gaps; Kwak and Han [8,9] used the transient liquid crystal

Contributed by the International Gas Turbine Institute (IGTI) of ASME for publication in the JOURNAL OF TURBOMACHINERY. Manuscript received October 1, 2003; final manuscript received March 1, 2004. IGTI Review Chair: A. J. Strazisar. Paper presented at the International Gas Turbine and Aeroengine Congress and Exibition, Vienna, Austria, June 13–17, 2004, Paper No. 2004-GT-69034.

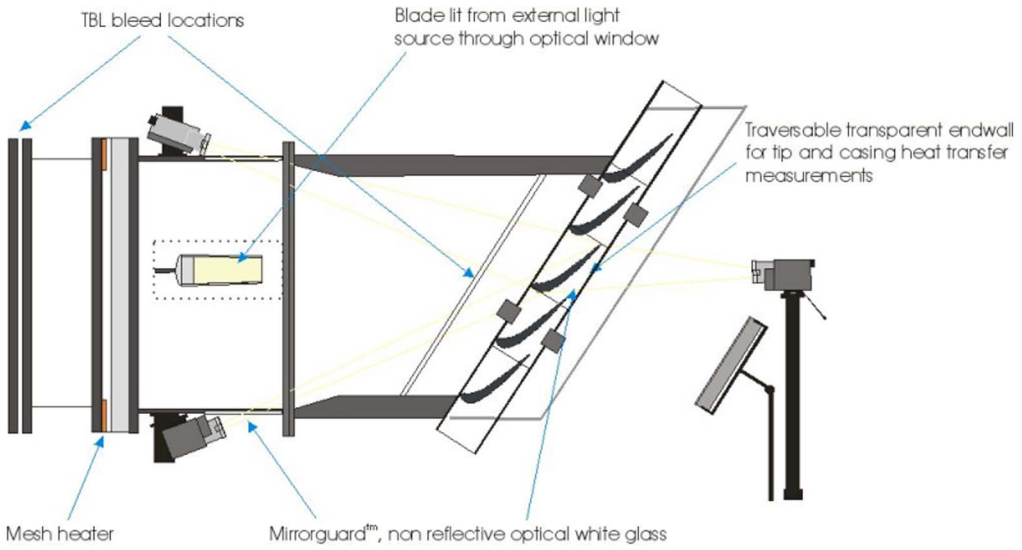

Fig. 1 Low speed cascade modified for heat transfer measurements

technique and Jin and Goldstein [10] the naphthalene technique to determine the effects of clearance gap, turbulence intensity and Reynolds number on the mass/heat transfer from the tip and near-tip surfaces.

This study explores the effects of introducing suction-side and cavity squealers. Film cooling is introduced at locations designed to optimize, in terms of both aerodynamics and heat transfer, the performance of the tip gap. Experimental measurements of heat transfer coefficient and film-cooling effectiveness using the transient liquid crystal technique are described. Pressure measurements, flow visualization and computational results are used to link the aerodynamic and heat transfer characteristics of the flow.

2 Experimental Procedure

The experiments were conducted in the Whittle Laboratory at the University of Cambridge. A schematic of the low-speed linear cascade is shown in Fig. 1. A variable-speed centrifugal fan was used to drive air through a five-blade cascade where it exits to atmosphere. Salient features of the cascade are listed in Table 1 and further detail is available in Heyes et al. [11], who used the same cascade. The blades were cantilevered from the "hub" by a screw arrangement that allows the tip clearance gap to be set. All measurements were made about the central blade in the cascade. The "casing" endwall could be interchanged with transparent windows providing optical access to the blade tip and aerofoil surfaces. The Reynolds number, based on exit velocity and chord, was 2.3×10^5.

The cascade has the same geometry as a two-stage HP version of the Peregrine (Hodson et al. [12]) which itself is based on an actual HP turbine. Three tip-gap geometries were tested: Plain tip, suction-side squealer, and cavity squealer. Referring to Fig. 2, two tip-gap heights, $H=3.7$ and 6.35 mm (1.6% and 2.8% chord) were used. The cavity and suction-side (SS) squealer geometries were designed in consultation with Siemens and Alstom, and based on the results of Part 1. The SS squealer was defined by offsetting the SS wall by 5 mm. The squealer starts on the chord line and continues until it meets with the pressure surface at the trailing edge. The cavity tip is characterized by offsetting the blade profile internally by 5 mm. At the trailing edge of the blade the cavity

Table 1 Details of low speed cascade

Chord, c	225 mm
Axial chord, C_x	103 mm
Pitch/chord ratio, s/C	0.824
Aspect ratio	2.11
Stage exit Re_c	2.3×10^5
Inlet flow angle, α_1	32.5°
Blade exit angle, α_2	75.6°
Practical tip clearance	3.7–6.35 mm
Mass flow rate	1.6 kg/s
Max thickness/chord	14%

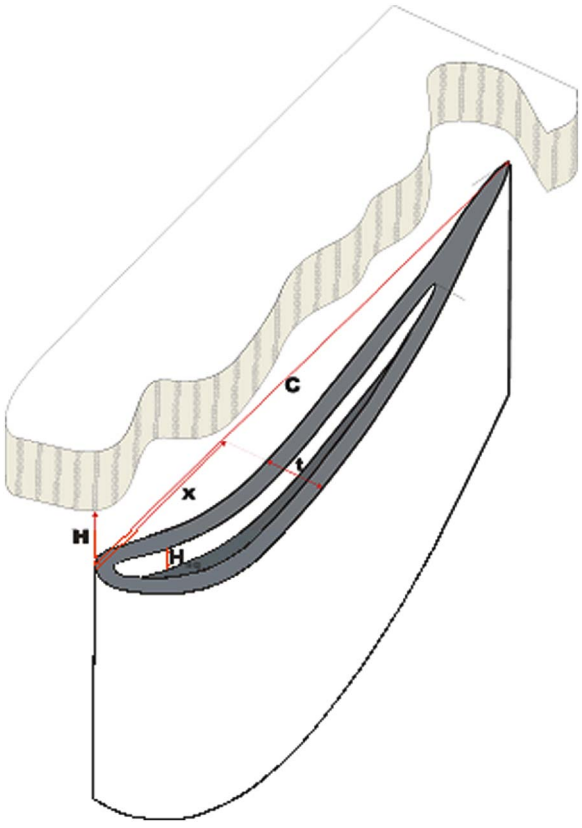

Fig. 2 Definition of blade parameters

closes at $x/C=0.75$ because it was machined using a 1 mm cutting tool. The squealers were sufficiently wide to provide some heat transfer data on their surface but thin enough to prevent reattachment. The cavity depth will affect the aerodynamics and heat transfer in the tip gap. The geometry and dimensions were based on a current Siemens design and on practical considerations. The cavity depth has not been considered as a parameter in this study. Note this is a three-dimensional (3D) study the ratio of cavity depth to gap varies with chord.

Most aerodynamic measurements were made on the casing but tip and aerofoil surface data was also available for the plain-tip geometry. The blade used for aerodynamic measurements was moulded from glass-fiber reinforced-epoxy in a CNC machined aluminium mould. During the moulding process a nylon string of 1 mm diameter was placed radially on the gel coat of the central blade. Once the epoxy set these strings were withdrawn and the resulting holes acted as pressure conduits for 16 subsequently drilled rows of chord-wise pressure tappings about the blade surface. Twenty-one cross-chord slots of 1 mm width were then milled into the tip interface, interfacing with the pressure-side conduits. These were used to gain tip pressure data using the micro tapping technique described by Bindon [13].

Static pressure data was also gathered using a traversing endwall. The endwall was traversed in a pitchwise direction using a computer-controlled stepper motor. Two rows of 21 pressure tapping holes located one blade pitch apart were used to measure endwall static pressure over the tip of the central blade and adjacent passages. All aerodynamic measurements were carried out using two cross-calibrated Scanivalve units.

The heat transfer experiments were performed on a polycarbonate replica of the cascade blades. Two replicas were made, a solid plain tip blade and a hollow blade with interchangeable tips for the film cooling and squealer investigations. Tip pieces were also constructed from Rhoacell, a low-conductivity machinable foam used to create an adiabatic surface. Heat transfer was measured using thermochromic liquid crystal (TLC). The method of analysis is described in the next section. Both narrow-band and wide-band liquid crystal were used. The color-play of the TLC was recorded with three digital video cameras. The traversing endwall used for pressure measurements was replaced with a similar polycarbonate endwall with an optical window. Optical access was also gained to the pressure and suction aerofoil surfaces as well as the leading edge. The use of a single narrow band crystal negated the potential errors associated with the viewing of TLC color-play under oblique lighting upon curved surfaces. To accurately remodel the blade surface from the three video feeds, the blade was marked with a radial grid which was used in an automated program to calculate camera angle. Due to the relatively large range of heat transfer rates measured, a number of experiments were performed at various nondimensional temperatures ($0.3<\theta<0.6$—see next section) to alleviate time errors at high heat transfer coefficients and conduction errors at low heat transfer coefficients.

There have been many published references regarding the effect of viewing angle on the calibration of both wide and narrow band TLC. Ireland and Jones [14] and Farina et al. [15] are good examples. The crystals used here were calibrated both in situ and using an isothermal copper-block calibration apparatus where the lighting and illumination angles were varied between 0 and 30 deg. This calibration method and apparatus is described in detail in Syson et al. [16]. Small uncertainties in the temperature obtained from the calibration were ±0.2 C. This amplifies to an uncertainty in heat transfer coefficient of approximately 3%, as explained by Owen et al. [17].

A hot mainstream flow was generated using an upstream wire mesh (Gillespie et al. [18]) powered by a 15 kW welder, shown in Fig. 3. Due to the large mass flow through the cascade (~2.8 kg/s), only the flow entering the tip gap was heated, the remaining flow passing through a cold mesh adjacent to the heater mesh. The heater mesh had a high aspect ratio of 6 and a thicker

Fig. 3 The mesh heater

than typical wire diameter was employed in order to reduce the mesh resistance such that the welder could deliver maximum power at 50 V DC. An aerofoil profile within the mesh assembly was used to help prevent the hot flow from mixing with the unheated flow. Traverse profiles indicated minimal mixing between the heated and unheated flows and a homogenous temperature profile entering the blade row. Boundary layer bleeds were implemented on the endwall to eliminate the thermal boundary layer. Area traverses upstream of the blade row have shown temperature field distortion within the region of interest to be less than 0.1 °C with the heater mesh on.

The mesh heater created an effective step-change in the air temperature immediately downstream, but at the cascade an exponential-type rise in air temperature was measured using a high-frequency thermocouple. A light emitting diode (LED) was used as a visual trigger to indicate the initialization of the welder, and hence the mesh, in the experiment. The distance between the mesh and the leading edge of the central blade divided by the flow velocity synchronised the thermocouple data and TLC color-play video. The time taken for the surface to locally reach a predetermined hue, corresponding to the maximum intensity of green light, was recorded and the thermocouple temperature history was resolved as a series of exponentials as described in the next section.

Film cooling experiments were performed using a single reservoir inside the blade. The temperature of the pressurised coolant flow was controlled carefully. Thermocouples and a total pressure probe were located inside the blade and three tubes insulated with Rhoacell, running through the length of the blade to holes in the hub, supplied coolant to the tip. A flow meter was used to gauge

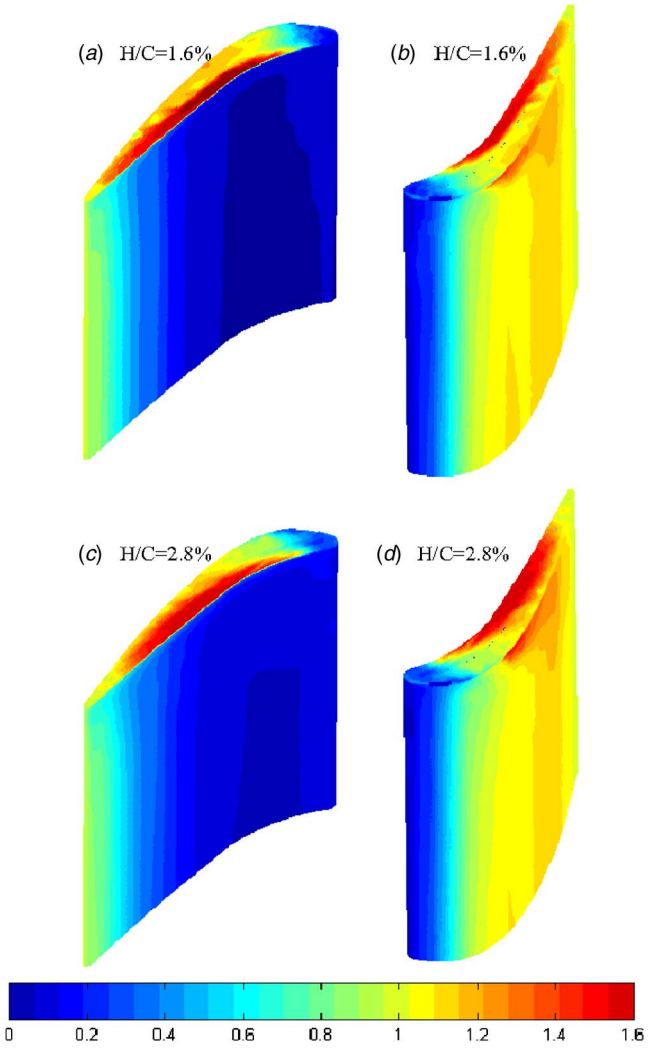

Fig. 4 C_p Contours as measured on the blade and tip

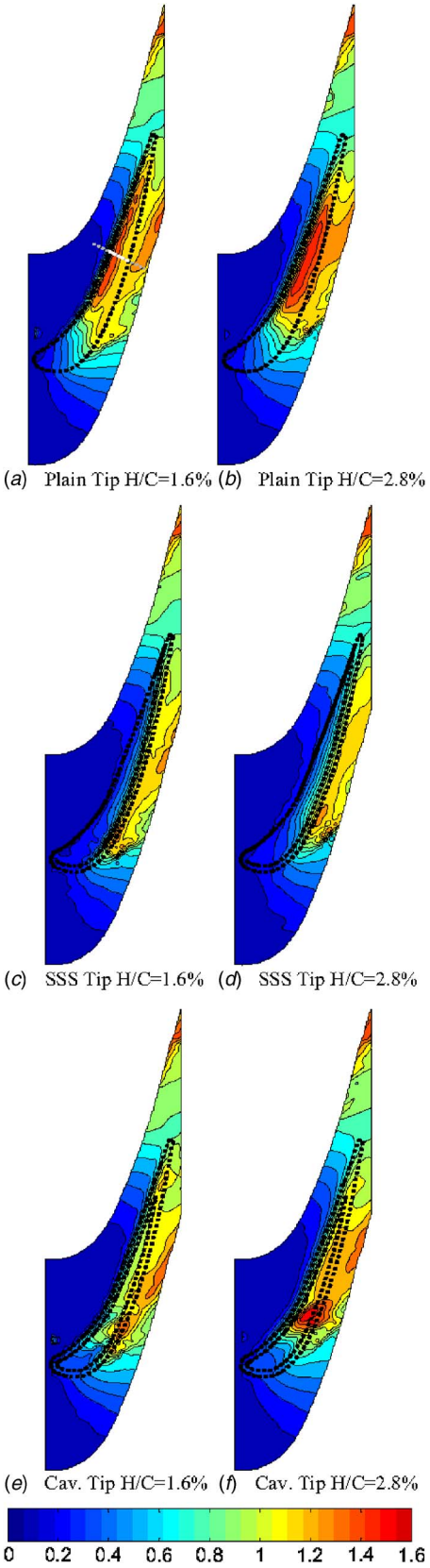

Fig. 5 C_p Contours as measured on the casing

the coolant flow rate. Each film-cooling hole was lined with 1 mm of Rhoacell to reduce two-dimensional (2D) conduction effects around the holes.

3 Transient Heat Transfer Technique

This section describes the experimental technique used to measure the heat transfer coefficient using themochromic liquid crystals. Further details of the theory are available in Shultz and Jones [19], Ireland and Jones [14] and Newton et al. [20].

The heat transfer coefficient, h, is defined as

$$q_w = h(T_{aw} - T_w) \tag{1}$$

where q_w is the surface heat flux from the air to the wall, T_w is the surface temperature of the wall, and T_{aw} is the adiabatic-wall temperature. T_{aw} depends on the total-temperature of the air, T_a, and, in cases where compressibility is an issue, on the fluid dynamics.

In a typical transient test, an abrupt change in air temperature is generated, and narrow-band TLC is used to determine the surface temperature, T_w, of the test piece. Knowing the time, t, at which the surface reaches T_w, h (assumed time-invariant) can be calculated from the solution of Fourier's one-dimensional conduction equation for the case of a semi-infinite plate.

In the tests reported here, the mesh heater created an effective step-change in the air temperature, but at the test section an exponential-type rise in air temperature was produced. Newton et al. [20] show that the adiabatic wall temperature, T_{aw}, could be fitted by an exponential series of m terms, such that

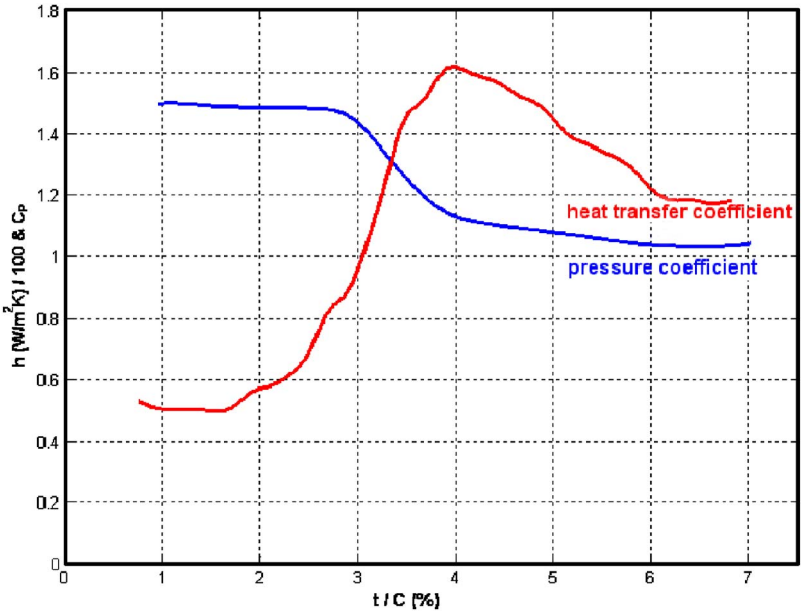

Fig. 6 Cross-chord measurements of C_p and h at $x/C=50\%$ $H/C=1.6\%$

$$T_{aw}(t) = T_{a,0} + \sum_{j=1}^{m} T_{a,j}(1 - e^{-t/\tau_j}) \tag{2}$$

where $T_{a,0}$ is the air temperature at $t=0$, $T_{a,j}$, and τ_j are the constant amplitudes and time-constants, respectively. As $t \to \infty$,

$$T_{aw,\infty} = T_0 + \sum_{j=1}^{m} T_{a,j} \tag{3}$$

where T_0 is the initial temperature of the wall, such that

$$T_0 = T_{a,0} \tag{4}$$

Fourier's conduction equation for a semi-infinite slab has been solved by Gillespie et al. [21] for the case where there is a simple exponential increase in the air temperature, corresponding to the case where $m=1$ in Eq. (3). The solution is

$$\theta = \frac{T_w - T_0}{T_{aw,\infty} - T_0} = g(\beta, \beta_\tau) \tag{5}$$

where

$$g(\beta,\beta_\tau) = 1 - \frac{1}{1+\beta_\tau^2} e^{\beta^2} \operatorname{erfc}(\beta) - e^{-t/\tau} \frac{\beta_\tau^2}{1+\beta_\tau^2} \times \left\{ 1 + \frac{1}{\beta_\tau} \left[\frac{1}{\pi} \sqrt{\frac{t}{\tau}} + \frac{2}{\pi} \sum_{n=1}^{\infty} \frac{1}{n} e^{-n^2/4} \sinh\left(n \sqrt{\frac{t}{\tau}} \right) \right] \right\} \tag{6}$$

$$\beta = \frac{h\sqrt{t}}{\sqrt{\rho c k}} \tag{7}$$

and

$$\beta_\tau = \frac{h\sqrt{\tau}}{\sqrt{\rho c k}} \tag{8}$$

For the case where $\tau=0$, Eq. (5) simplifies to

$$\theta = f(\beta) \tag{9}$$

where, from Eq. (6)

$$f(\beta) = 1 - e^{\beta^2} \operatorname{erfc}(\beta) \tag{10}$$

which is the well-known solution of Fourier's equation for a step-change in the air temperature.

The general solution for an exponential series, corresponding to Eq. (3), is given by Newton et al. [20] as

$$\theta = \sum_{j=1}^{m} \frac{T_{a,j}}{T_{aw,\infty} - T_0} g(\beta, \beta_{\tau j}) \tag{11}$$

For the special case where $m=1$, $T_{a,1}=T_{aw,\infty}-T_0$ and Eq. (11) reduces to (6).

The presence of cooling, i.e., injected air at a second temperature T_c, introduces the film cooling effectiveness, $\eta=(T_{aw}-T_c)/(T_a-T_c)$ as a variable in addition to h. Like h, it is assumed that η is only a function of the aerodynamics and time invariant.

The cooled heat transfer measurements were performed in two stages. Film cooling effectiveness was measured on a Rhoacell tip with the wide-band TLC. Heat transfer coefficient was then obtained by a separate experiment using a narrow-band crystal and polycarbonate tip. The heat transfer coefficient was deduced using the local measured η.

In order to evaluate the influence of the coolant in an engine environment a net heat flux reduction (NHFR) similar to that used by Sen et al. [22] is used. The NHRF is the ratio of the reduction in heat flux due to film cooling to the heat flux without cooling:

$$\Theta_E = \frac{T_a - T_c}{T_r - T_w} \tag{12}$$

$$\mathrm{NHFR} = \frac{q_w - q_{w,c}}{q_w} = 1 - \frac{h_c}{\overline{h_{uc}}}(1 - \eta\Theta_E) \tag{13}$$

Here $\overline{h_{uc}}$ is the mean uncooled heat transfer coefficient. The objective of film cooling is to increase NHFR by reducing heat transfer coefficient and increasing η. The NHFR is most meaningful at engine-representative conditions. The value of θ_E was selected as 1.5, comparable to that of Sargison et al. [23] and based on an air total temperature $T_a=1900$ K, a blade metal temperature $T_w=1200$ K, a coolant total temperature $T_c=880$ K, and a transonic air recovery temperature $T_r=1880$ K. An integrated average of the NHFR may be used to determine the overall performance of

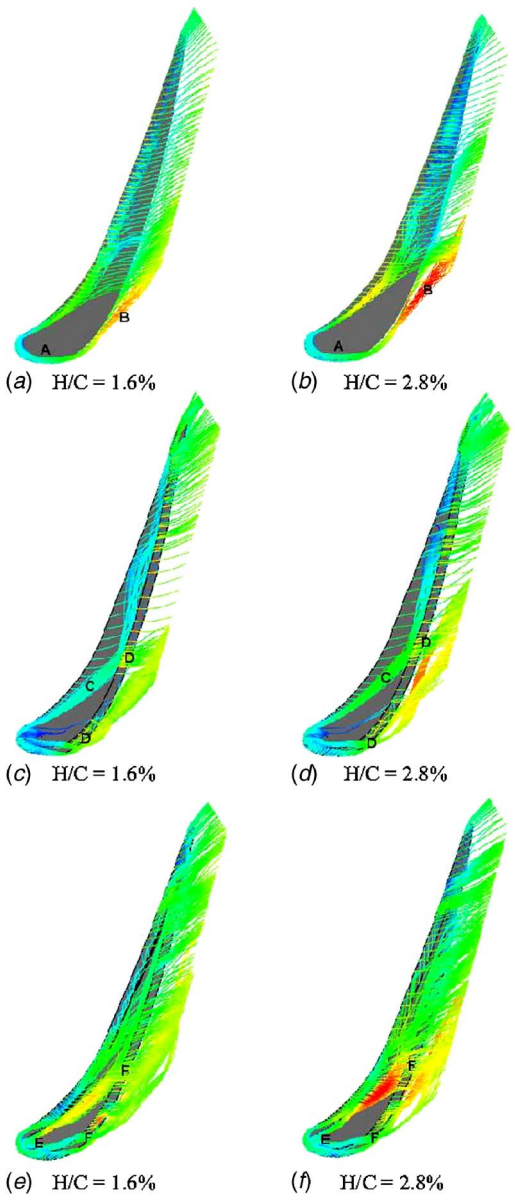

Fig. 7 CFX flow visualization

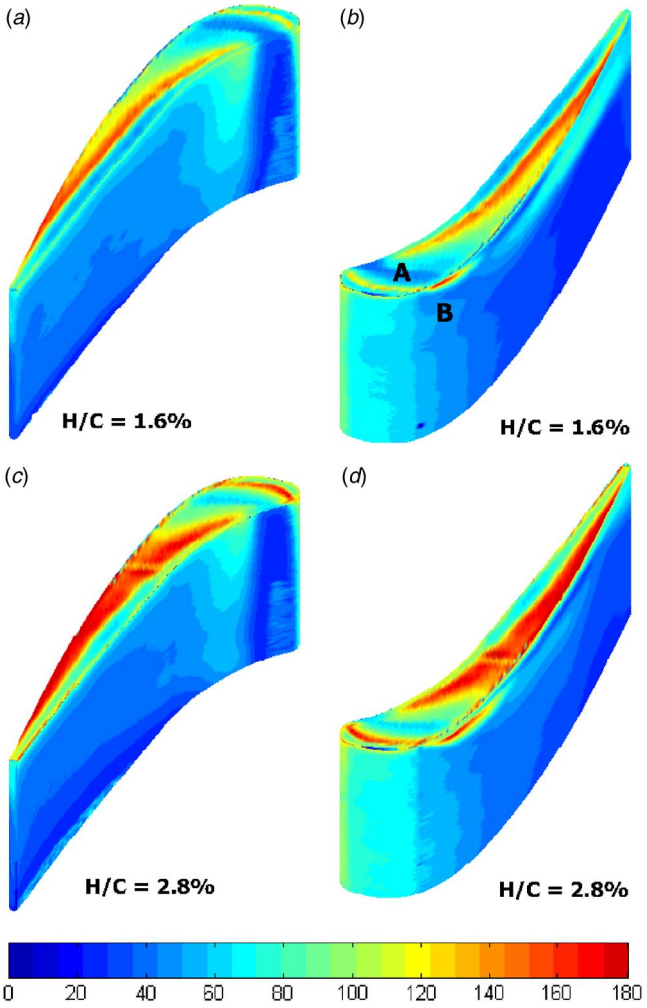

Fig. 8 Heat transfer coefficients for plain tip geometry: Top *H/C* 1.6%, bottom *H/C*=2.8%

a cooled geometry by means of a summation over all $i=1$ to n pixels:

$$\overline{\mathrm{NHFR}} = 1 - \frac{1}{n \cdot \overline{h_{uc}}} \sum_{i=1}^{n} h_{c,i}(1 - \eta\Theta_E) \tag{14}$$

4 Experimental Results

The experimental results are divided into two main sections: Aerodynamic (pressure) and heat transfer (temperature) results. Three geometries, at two gap heights, were tested: Plain tip, suction-side squealer, and cavity. Most aerodynamic measurements are made on the casing—tip and aerofoil surface data is only available for the plain-tip geometry. In contrast, the heat transfer data has only been gathered on the tip, with aerofoil data only presented for the plain-tip case. The experiments are supported by flow visualization information computed using the CFX code.

Aerodynamic Measurements for the Plain Tip. Figures 4(*a*)–4(*d*) show measurements of the pressure coefficient, C_p, on the plain tip blade as well as data on the suction and pressure aerofoil surfaces at clearance heights of 3.7 and 6.35 mm (H/C =1.6% and 2.8%, respectively). Note that only 33% of the blade span is shown. These figures clearly illustrate that between $0.2 < x/C < 0.9$ there is a region of high velocity associated with the flow separating from the pressure-side edge of the tip gap. The flow subsequently decelerates as it reattaches to the tip surface before reaching the suction surface. Figures 5(*a*) and 5(*b*) show the corresponding C_p measured on the casing, indicating similar features. A region of relatively low leakage velocity is observed near the leading edge of the blade tip, $x/C<0.2$, where there is less pressure differential to drive flow across the gap.

Figure 6 shows C_p plotted on the tip along a line perpendicular to the chord, which is approximately along the line of leakage trajectory, at $x/C=50\%$. The blade tip is approximately 9% of chord thickness at this location. The pressure data illustrates the presence of a separation bubble with reattachment approximately a third of the distance along the cross-chord line following the acceleration-deceleration through the vena contracta. High heat transfer coefficient is observed where the flow reattaches.

Flow reattachment is indicated by an abrupt decrease in the rate of deceleration on the tip. The red-yellow contour divides in Fig. 4 provide an approximate indication of the reattachment line.

It is evident that with the larger clearance gap, the region of separation increases, as reported widely (for example, Heyes et al., [11]). The leakage flow is accompanied by a small acceleration on the pressure-side aerofoil surface in the immediate vicinity

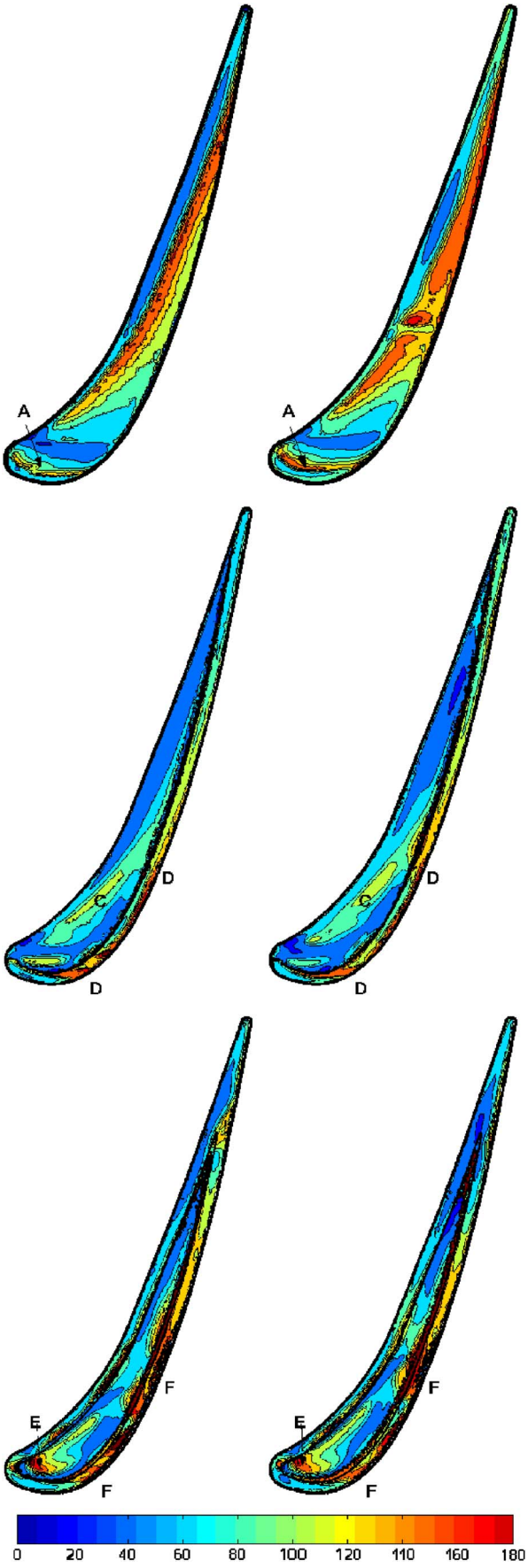

Fig. 9 Heat transfer coefficient for plain (top pair), squealer (middle) and cavity (bottom) geometries (W/m^{2}K)

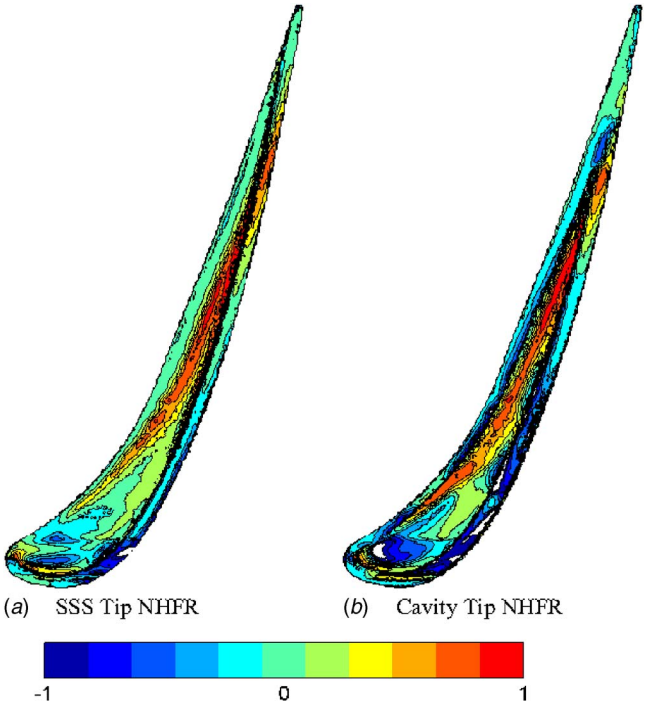

Fig. 10 Uncooled tip NHFR for $H/C=1.6\%$

of the gap, which is accentuated in the larger tip gap. The impingement of the leakage vortex is visible on the suction-side aerofoil surface. The intensity of the leakage vortex is observed to increase in intensity as clearance gap increases.

Figures 7(*a*) and 7(*b*) illustrate the trajectory of leading-edge streamlines, obtained by CFX, for the case of the plain tip. The streamlines are color-coded to mark velocity. The flow visualization predictions support the experimental data, indicating high leakage velocities in the regions of high C_p. The CFD has captured the pressure-side separation discussed above and also reveals a similar separation near the leading edge of the blade ($x/c=0$), marked A where flow is driven into the tip gap by high pressure near the stagnation point of the blade. The highest velocities are calculated in the tip-leakage vortex on the suction side of the tip, marked B in the two figures. The strength of this vortex is observed to increase as the gap width increases.

Aerodynamic Measurements for SS-Squealer and Cavity Tip. Figures 5(*c*) and 5(*d*) show measurements of C_p on the casing for flow through the gap with suction-side squealer. The corresponding CFD streamlines are shown in Figs. 7(*c*) and 7(*d*). High C_p at and downstream of the squealer ridge is observed where the reduced area at the squealer causes an abrupt acceleration. Although the flow again separates off the pressure-side corner of the tip, the CFD streamlines indicate that reattachment is mainly associated with a swirling vortical flow within the pressure-side separation bubble. This flow, driven along its axis by the chordwise pressure gradient, impinges on the foremost, thicker portion of the tip (marked C) and on the squealer at two positions marked D in Figs. 7(*c*) and 7(*d*). Enhanced heat transfer is expected at these locations. The first position is near the leading edge of the blade while the second is at $x/C\approx0.30$. The vortical flow is more intense for the larger gap and the second point of impingement is further along the chord line at $x/C\approx0.35$.

Heat Transfer Measurements for Plain Tip. Figures 8(*a*)–8(*d*) show measurements of the heat transfer coefficient on the plain tip blade as well as data on the suction and pressure aerofoil surfaces at clearance heights of 3.7 and 6.35 mm ($H/C=1.6\%$ and 2.8%, respectively). Note that only 25% of the blade

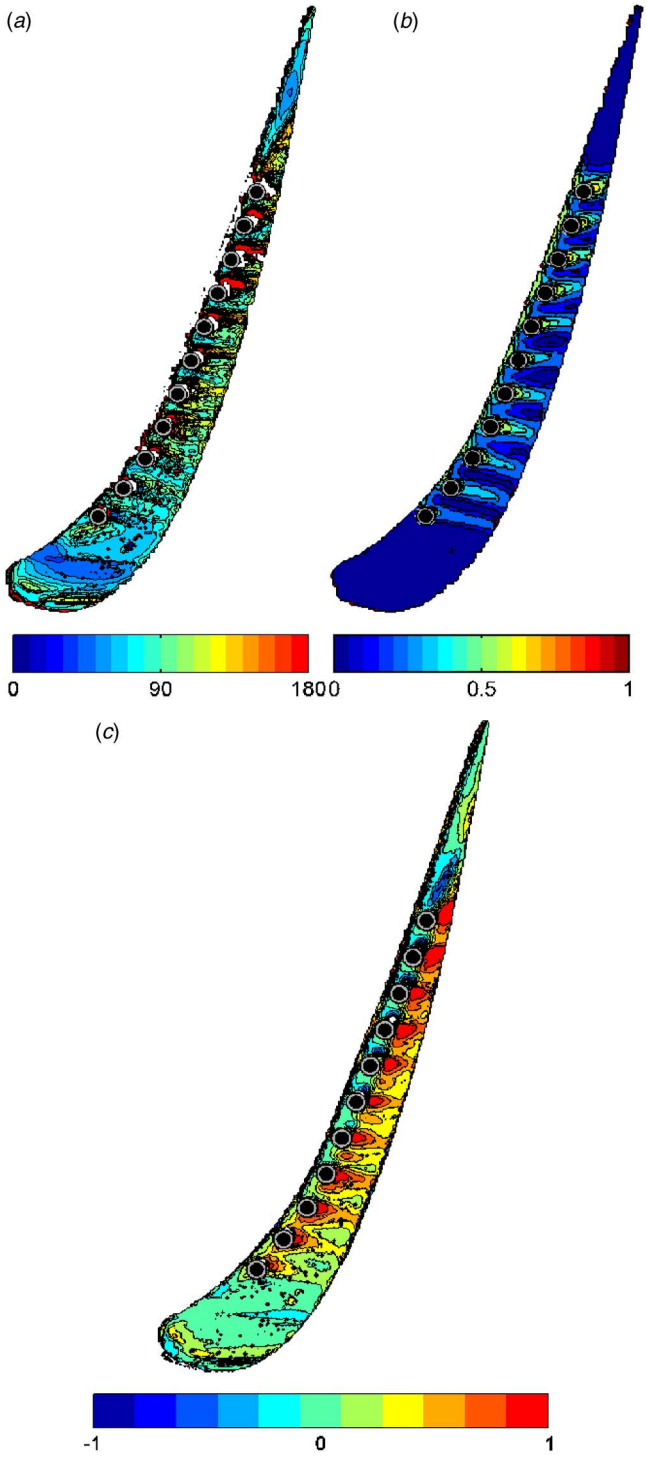

Fig. 11 (*a*)–(*c*). Cooled Tip *h*, η and NHFR

span is shown. The most striking observation is that the highest heat transfer coefficient on any surface (including the stagnation region on the pressure and suction aerofoil surfaces) is observed on the tip of the blade!

The associated pressure field and CFD flow visualization are shown in Figs. 4(*a*)–4(*d*), 7(*a*), and 7(*b*). It is observed that the maximum heat transfer coefficient occurs in the region of reattachment on the blade tip essentially along a line parallel to the pressure-side rim. This region is more extensive for the larger tip gap, though the peak values of *h* are similar. Figure 6(*b*) shows *h* plotted on the tip along a line perpendicular to the chord, which is approximately along the line of leakage trajectory, at $x/c=50\%$. The blade tip is approximately 9% of chord thickness at this location. Comparison with Fig. 6(*a*) does indeed indicate that the high heat transfer coefficient is located where the flow reattaches.

A ridge of high heat transfer is also observed near the leading-edge of the blade (marked A in Figs. 8(*b*) and 8(*d*)) where flow which is driven into the tip gap by high pressure near the stagnation point of the blade, separates and then reattaches (see A in Figs. 7(*a*) and 7(*b*)). Generally there is low heat transfer in this leading edge region where there is less pressure differential to drive flow across the gap.

The impingement of the tip-leakage vortex (marked B in Figs. 7(*a*), 7(*b*), and 8(*b*)–8(*d*)) is visible on the suction-side aerofoil surface where high heat transfer is observed. The area of the region influenced the leakage vortex is observed to increase as the intensity of the vortex increases with the increase in clearance gap. It is interesting to note that the origin of the leakage vortex appears to be the flow over the leading edge of the suction surface.

Heat Transfer Measurements for SS-Squealer and Cavity Tip. Figures 9(*c*)–9(*f*) show contours of heat transfer coefficient on the blade tip for the suction-side squealer and cavity geometries, respectively. Note Figs. 9(*a*) and 9(*b*) shows the heat transfer for the plain tip again for comparison. It is immediately evident that both the suction-side squealer and cavity squealer have eliminated the peak in heat transfer associated with the intense fluid-dynamic effect of flow reattachment exhibited by the plain tip. However, the suction-side squealer features locations of high local heat transfer at positions marked C and D. The corresponding CFD streamlines are shown in Figs. 7(*c*) and 7(*d*) and the locations where flow is observed to impinge on the tip and squealer (also marked C and D) correlate well with these positions of high heat transfer. The cavity squealer also features local spots of high heat transfer (marked F), which correspond well to the flow impingement marked in the flow visualization, Figs. 7(*e*) and 7(*f*). In addition, high heat transfer is observed at the base of the squealer at position *E*, possibly associated with the vortical flow drawing fluid into the cavity. The heat transfer in both the suction-side squealer and cavity squealer are relatively insensitive to the tip-gap clearance.

Figures 10(*a*) and 10(*b*) show the NHFR for the suction-side and cavity squealer for the case of a $H/C=1.6\%$. No film cooling is present and so here the NHFR is based on the local heat transfer coefficient compared with that measured using the plain tip, i.e., $\mathrm{NHFR}=1-h/h_{\text{plain-tip}}$. Regions of positive NHFR in Figs. 11(*a*) and 11(*b*) indicate a beneficial influence of the squealer geometry while regions of negative NHFR indicate an increase in heat transfer. An integrated average of the NHFR for the suction-side squealer was calculated as 0.15, suggesting a reduction of 15% in heat flux. The integrated NHFR for the cavity squealer was 0.0, indicating no net overall benefit at this tip-gap height.

Cooled Heat Transfer Measurements on Plain Tip. The squealer geometries are one method that can be used to reduce the heat transfer on the tip of the blade. An alternate method is to use film cooling. A coolant configuration was designed, based on the data collected on the uncooled tip. The coolant holes were located at 5 mm from the pressure-side corner in a cross chord direction, in order to inject coolant into the separation bubble. The holes spanned from 15% to 70% chord to coincide with the regions of heightened heat transfer. This had the secondary benefit of avoiding the regions of high static pressure at the leading edge of the blade which would have resulted in coolant ingestion at low blowing rates. The coolant hole diameter was 4 mm which scales to engine representative film cooling geometries, as suggested by Siemens and Alstom. Note that a coolant mass flow equal to 1% of the mainstream flow is typically used in the turbine.

Figures 11(*a*)–11(*c*) illustrate cooling data for a plain tip for the case of $H/C=1.6\%$. The average coolant blowing rate was 0.9,

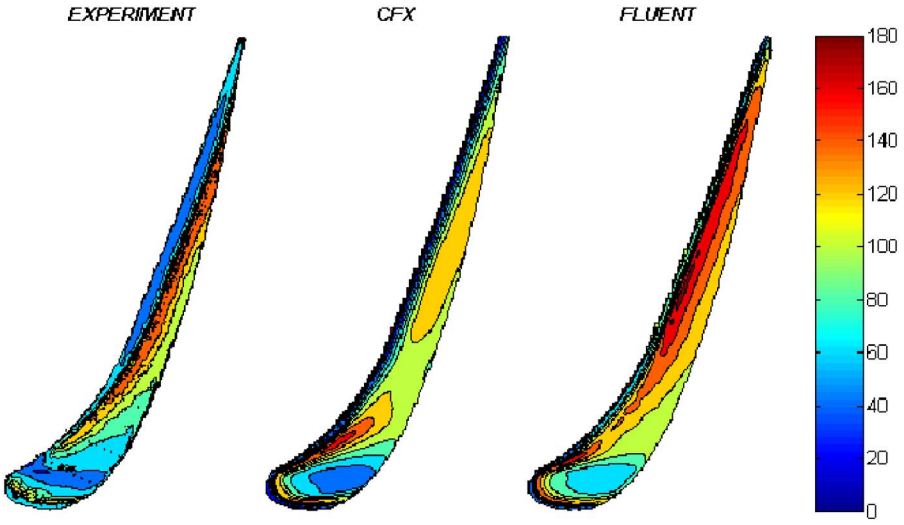

Fig. 12 CFD predictions of h (W/m^2K) for plain tip, $H/C=1.6\%$

which corresponded to a coolant mass flow equal to 0.5% of the mainstream flow—a percentage not untypical of that used in engineering practice. Note Fig. 9(*a*) is the equivalent map for the uncooled tip. These figures show contours of heat transfer coefficient, film cooling effectiveness and local NHFR on the cooled tip. The holes have been positioned to inject coolant into the separation bubble and this has successfully avoided the high heat transfer associated with reattachment present in the uncooled case. There are, however, some regions of high local heat transfer coefficient near the holes due to the fluid-interaction between the coolant and mainstream. The cooling footprints shown in the effectiveness plot indicate that the flow is essentially perpendicular to the chord and that the coolant remains attached.

The NHFR provides a quantification of the reduction in heat transfer to the tip with film cooling compared to that heat transfer without cooling. The objective of film cooling is to increase NHFR by reducing heat transfer coefficient and increasing effectiveness. Regions of positive NHFR in Fig. 10(*c*) indicate a beneficial influence of the coolant and these are predominantly located in the cooling footprints. Some regions of negative NHFR are observed in areas where the effectiveness is low but the heat transfer coefficient has been elevated due to increased turbulent mixing with the cooling present. Away from the cooling holes the NHFR is near zero. An integrated average of the NHFR, defined by Eq. (14), was calculated as 0.33, indicating an effective cooling design. For a given blade tip geometry and mainstream flow conditions, the NHFR is a function of the cooling-hole locations as well as the coolant blowing rate. Only one case has been reported here but a positive integrated NHFR resulted for all cases where the coolant was injected into the separation bubble on the tip.

Predicted heat transfer coefficients for the uncooled plain tip for the case of $H/C=1.6\%$ are shown in Fig. 12. These calculations were performed using two commercial codes: FLUENT and CFX. These calculations are shown to be in good qualitative agreement with the experiments and have captured all of the flow features described in the above discussion.

5 Conclusions

Contours of heat transfer coefficient have been measured on the tip of a generic turbine blade as well as on the aerofoil suction and pressure surfaces near the tip. The experiments were conducted at an exit Reynolds number $=2.3\times10^5$ in a five-blade linear cascade using the transient liquid crystal technique. Tip clearances of 1.6% and 2.8% chord and three different tip geometries were used. These measurements were supported by pressure measurements on the tip and casing and by flow visualization calculated using CFX.

The highest heat transfer coefficients on any surface (including the stagnation region on the pressure and suction aerofoil surfaces) were observed on the tip of the blade. The pressure and flow visualization revealed that the flow through the plain tip gap was governed by a separation bubble near the pressure-side entrance to the gap. The leakage flow separated from the tip surface and reattached in a region parallel to the pressure-side rim. The highest heat transfer coefficients were located in this region. A ridge of high heat transfer was also observed near the leading edge where flow which is driven into the tip gap by high pressure near the stagnation point of the blade, separates and then reattaches. Generally there is low heat transfer in this region where there is less pressure difference to drive flow across the gap. The impingement of the leakage vortex is visible on the suction-side aerofoil surface where high heat transfer is also observed. This feature was also captured clearly by the flow visualization. The area of the region influenced by the leakage vortex was observed to increase as the vortex became more intense with an increase in clearance gap.

Both squealer geometries eliminated the peak in heat transfer associated with flow reattachment from the pressure-side rim which dominated the case of the plain tip. However, high local heat transfer was observed at positions on the squealers which corresponded to areas of impingement. The cavity squealer also featured local spots of high heat transfer at the base of the squealer near the leading edge, possibly associated with vortical flow drawing fluid into the cavity. The areas of high measured heat transfer correlated well with the locations of impingement determined by the calculated flow visualization. The suction-side squealer featured an integrated net heat flux reduction (NHFR) of 0.15 while the cavity squealer revealed no net heat flux reduction.

Film cooling holes were introduced on the plain tip along a line 5 mm from the pressure-side corner in a cross chord direction in order to inject coolant into the separation bubble. This successfully eliminated the high heat transfer associated with reattachment present in the uncooled case. Measurements of heat transfer coefficient and cooling effectiveness led to a calculation of the NHRF on the blade tip. An integrated average of the NHFR, calculated that the net heat flux to the tip at engine-level temperatures would be reduced by 33% (for a coolant mass flow equivalent to 0.5% of the mainstream), indicating an effective cooling design.

Nomenclature

B = blowing rate, $B=\rho_c v_c/\rho_a v_a$
C = specific heat of wall
C = chord, 225 mm
C_p = pressure coefficient, $C_p=(P_t-P)/(P_t-P_e)$
$f(\beta)$ = step-change solution of Fourier's equation
$g(\beta,\beta_\tau)$ = exponential solution of Fourier's equation
h = heat transfer coefficient $(q_w/(T_{aw}-T_w))$
H = tip clearance gap
H_{sq} = squealer height
k = thermal conductivity of wall
m = number of terms in exponential series
NHRF = net heat flux reduction, $\text{NHFR}=(q_w-q_{w,c})/q_w$
P = pressure
q_w = heat flux from air to wall
t = time, blade thickness
T = temperature
v = free-stream velocity
x = distance along chord
β = parameter in step-change solution $\beta=(h\sqrt{t/\rho ck})$
β_τ = parameter in exponential solution $\beta_\tau=(h\sqrt{\tau/\rho ck})$
ρ = density
η = film cooling effectiveness, $\eta=(T_{aw}-T_c)/(T_a-T_c)$
θ = nondimensional temp. $\theta=(T_w-T_0)/(T_{aw,\infty}-T_{w0})$
Θ_E = ND engine. temp $\Theta_E=(T_a-T_c)/(T_r-T_w)$
τ = time constant

Subscripts

0 = value at $t=0$
∞ = value as $t\rightarrow\infty$
a = mainstream air
aw = adiabatic wall
c = coolant, cooled
e = cascade exit
j = jth term in series
r = recovery
t = upstream stagnation condition
uc = uncooled

References

[1] Booth, T. C., Dodge, P. R., and Hepworth, H. K., 1982, "Rotor Tip Leakage: Part 1; Basic Methodology," ASME J. Eng. Power, **104**, pp. 154–161.
[2] Mayle, R. E., and Metzger, D. E., 1986, "Heat Transfer at the Tip of an Unshrouded Turbine Blade," *Proceedings, Seventh International Heat Transfer Conference*, Vol. 3, pp. 87–92.
[3] Srinivasan, V., and Goldstein, R. J., 2003, "Effect of Endwall Motion on Blade Tip Heat Transfer," ASME J. Turbomach., **125**, pp. 267–273.
[4] Bunker, R. S., 2001, "A Review of Turbine Blade Tip Heat Transfer, Heat Transfer in Gas Turbine Systems," Ann. N.Y. Acad. Sci., **934**, pp. 64–79.
[5] Kim, Y. W., and Metzger, D. E., 1993, "Heat Transfer and Effectiveness on Film Cooled Turbine Blade Tip Models," ASME Paper No. 93-GT–208.
[6] Chen, G., Dawes, W. N., and Hodson, 1993, "A Numerical and Experimental Investigation of Turbine Tip Gap Flow," 29th Joint Propulsion Conference and Exhibit, AIAA Paper No. 93-2253.
[7] Bunker, R. S., Bailey, J. C., and Ameri, A. A., 1999, "Heat Transfer and Flow on the First Stage Blade Tip of a Power Generation Gas Turbine. Part I: Experimental Results," ASME Paper No. 99-GT-169.
[8] Kwak, J. S., and Han, J. C., 2002, "Heat Transfer Coefficient and Film-Cooling Effectiveness on a Gas Turbine Blade Tip," ASME Paper No. GT-2002-30194.
[9] Kwak, J. S., and Han, J. C., 2002, "Heat Transfer Coefficient and Film-Cooling Effectiveness on the Squealer Tip of a Gas Turbine Blade," ASME Paper No. GT-2002-30555.
[10] Jin, P., and Goldstein, R. J., 2002, "Local Mass/Heat Transfer on Turbine Blade Near-Tip Surfaces," ASME Paper No. GT-2002-30556.
[11] Heyes, F. J. G., Hodson, H. P., and Dailey, G. M., 1991, "The Effect of Blade Tip Geometry on the Tip Leakage Flow in Axial Turbine Cascades," ASME Paper No. 91-GT-135.
[12] Hodson, H. P., Banieghbal, M. R., and Dailey, G. M., 1995, "Three-Dimensional Interactions in the Rotor of an Axial Turbine," AIAA J. Propul. Power, **11**(2), pp. 196–204.
[13] Bindon, J. P., 1989, "The Measurement and Formation of Tip Clearance Loss," ASME J. Turbomach., **111**, pp. 257–263.
[14] Ireland, P. T., and Jones, T. V., 2000, "Liquid Crystal measurements of Heat Transfer and Surface Shear Stress," Meas. Sci. Technol., **11**, pp. 969–986.
[15] Farina, D. J., Hacker, J. M., Moffat, R. J., and Eaton, K., 1993, "Illuminant Invariant Calibration of Thermochromic Liquid Crystals," *Visualization of Heat Transfer Processes*, American Society of Mechanical Engineers, Heat Transfer Division, Vol. 252, pp. 1–11.
[16] Syson, B. J., Pilbrow, R. G., and Owen, J. M., 1996, "Effect of Rotation on Temperature Response of Thermochromic Liquid Crystal," Int. J. Heat Fluid Flow, **17**, pp. 491–499.
[17] Owen, J. M., Newton, P. J., and Lock, G. D., 2003, "Transient Heat Transfer Measurements Using Thermochromic Liquid Crystal. Part 2: Experimental Uncertainties," Int. J. Heat Fluid Flow, **24**, pp. 23–28.
[18] Gillespie, D. R. H., Wang, Z., and Ireland, P. T., 2001, "Heater element," European Patent No. 0847679.
[19] Schultz, D. L., and Jones, T. V., 1973, "Heat Transfer Measurements in Short Duration Hypersonic Facilities," Paper No. AGARD-AG-165.
[20] Newton, P. J., Yan, Y., Stevens, N. E., Evatt, S. T., Lock, G. D., and Owen, J. M., 2003, "Transient Heat Transfer Measurements Using Thermochromic Liquid Crystal. Part 1: An Improved Technique," Int. J. Heat Fluid Flow, **24**, pp. 14–22.
[21] Gillespie, D. R. H., Wang, Z., Ireland, P. T., and Kohler, S. T., 1998, "Full Surface Local Heat Transfer Measurements in a Model of an Integrally Cast Impingement Cooling Geometry," ASME J. Turbomach., **120**, pp. 92–99.
[22] Sen, B., Schmidt, D. L., and Bogard, D. G., 1994, "Film Cooling with Compound Angle Holes: Heat Transfer," ASME Paper No. 94-GT-311.
[23] Sargison, J. E., Guo, S. M., Oldfield, M. L. G., Lock, G. D., and Rawlinson, A. J., 2002, "A Converging Slot-Hole Film-Cooling Geometry—Part 2: Transonic Nozzle Guide Vane Heat Transfer and Loss," ASME J. Turbomach., **124**, pp. 461–471.